

## Supernova Ejecta with Crystalline Silicate Dust in the Supernova Remnant MSH 15–52

HYUN-JEONG KIM,<sup>1,2</sup> BON-CHUL KOO,<sup>3</sup> AND TAKASHI ONAKA<sup>4</sup>

<sup>1</sup>*Department of Earth Science Education, Kongju National University  
56 Gongjudaehak-ro, Gongju-si, Chungcheongnam-do 32588, Republic of Korea*

<sup>2</sup>*Korea Astronomy and Space Science Institute*

*776 Daedeok-daero, Yuseong-gu, Daejeon 34055, Republic of Korea*

<sup>3</sup>*Department of Physics and Astronomy, Seoul National University*

*1 Gwanak-ro, Gwanak-gu, Seoul 08826, Republic of Korea*

<sup>4</sup>*Department of Astronomy, Graduate School of Science, The University of Tokyo  
7-3-1 Hongo, Bunkyo-ku, Tokyo 113-0033, Japan*

### ABSTRACT

IRAS 15099-5856 in the young supernova remnant (SNR) MSH 15–52 is the first and only SNR-associated object with crystalline silicate dust detected so far, although its nature and the origin of the crystalline silicate are still unclear. In this paper, we present high-resolution mid-infrared (MIR) imaging observations of the bright central compact source IRS1 of IRAS 15099-5856 to study the spatial distributions of gas and dust and the analysis of its Spitzer MIR spectrum to explore the origin of IRS1. The MIR images obtained with the T-ReCS attached on the Gemini South telescope show a complicated, inhomogeneous morphology of IRS1 with bright clumps and diffuse emission in [Ne II] 12.81  $\mu\text{m}$  and Qa 18.30  $\mu\text{m}$ , which confirms that IRS1 is an extended source externally heated by the nearby O star Muzzio 10, a candidate for the binary companion of the progenitor star. The Spitzer MIR spectrum reveals several ionic emission lines including a strong [Ne II] 12.81  $\mu\text{m}$  line, but no hydrogen line is detected. We model the spectrum using the photoionization code CLOUDY with varying elemental composition. The elemental abundance of IRS1 derived from the model is close to that of SN ejecta with depleted hydrogen and enhanced metals, particularly neon, argon, and iron. Our results imply that IRS1 originates from the SN ejecta and suggest the possibility of the formation of crystalline silicate in newly-formed SN dust.

*Keywords:* Infrared spectroscopy(2285) — Supernova remnants(1667) — Interstellar medium(847)

### 1. INTRODUCTION

Silicates are the most common dust species in the interstellar medium (ISM) of galaxies. While silicate dust in the ISM of our Galaxy is indicated to be mostly amorphous (Kemper et al. 2004; Gordon et al. 2023), a sign of crystalline silicate has also been suggested (Do-Duy et al. 2020). Crystalline silicates have so far been detected in evolved stars and young stars (e.g., Molster et al. 1999a; Malfait et al. 1999). Crystallization of amorphous silicate grains is suggested to occur in circumstellar disks (Molster et al. 1999b), and several hypotheses of the formation of crystalline silicate have

been proposed including the radial mixing in the disk and shock waves (e.g., Maaskant et al. 2015, references therein). Crystalline silicate has been also detected in ultraluminous infrared galaxies with the crystalline-to-amorphous silicate mass ratios of  $\sim 0.1$  (Spoon et al. 2006). This suggests that supernovae (SNe) may be a source of crystalline silicates, leading to a model of evolution of crystalline silicates in galaxies (Kemper et al. 2011). Kemper et al. (2011) propose a model of silicate dust evolution in the galaxy that crystalline silicate is formed in SNe and amorphized by cosmic-ray hits, suggesting that the crystalline silicate features could be a useful measure of the youthfulness of the galaxy.

However, the formation of silicate dust in SNe is uncertain. Past observations in near-infrared (NIR) to mid-infrared (MIR) have revealed the newly-formed

dust in the ejecta of core-collapse SNe although the detected dust mass is smaller by more than two orders of magnitude than the mass theoretically predicted (e.g., Sugerma et al. 2006; Sakon et al. 2009; Szalai et al. 2011). Most of the SN dust have not shown the  $10\ \mu\text{m}$  silicate feature, suggesting that they are mostly carbonaceous dust, and only a few SNe show evidence for the formation of silicate dust (Kotak et al. 2009; Shahbandeh et al. 2023). On the other hand, an appreciable amount of dust has been detected in SN 1987A and young supernova remnants (SNRs) from far-infrared (FIR) observations (e.g., Matsuura et al. 2011; Chawner et al. 2020; Millard et al. 2021), but dust composition could not be derived because strong dust features are only present in MIR. From MIR spectroscopic observations of SNRs, the presence of carbonaceous dust is suggested (e.g., Tappe et al. 2006; Andersen et al. 2011), and some SNRs show an indication of silicate dust including unusual non-stoichiometric silicate and metal oxides (e.g., Arendt et al. 2014; Temim et al. 2017; Rho et al. 2018). But there has thus far not been any observational evidence for the presence of crystalline silicate in SNe or SNRs except for one case, MSH 15–52 (G320.4-1.2), for which its association with the SN explosion is not yet clearly understood.

MSH 15–52 is a young, core-collapse SNR with a complex morphology composed of the central pulsar wind nebula and a large radio shell with two distinctive components to northwest and southeast separated about 40 pc at a distance of  $5.2 \pm 1.4$  kpc (Gaensler et al. 1999, 2002, but see below). Although there is no obvious radio counterpart to the pulsar wind nebula, the extended X-ray nebula in which the pulsar is embedded appears to coincide in position and morphology of the radio components, supporting their association (Gaensler et al. 1999). From the large extent of the SNR compared to the young age of 1,700 yrs estimated by the central pulsar PSR B1509-58 (Seward et al. 1983), it was suggested that MSH 15–52 is the remnant of Type Ib SN (SN Ib) with a relatively small amount of SN ejecta and that the progenitor of the SNR was in a binary system with the O star Muzzio 10 (2MASS J15135520-5907516) which is  $\sim 20''$  apart from the pulsar (Gaensler et al. 1999). In the SNR, close to the pulsar, a bright MIR source IRAS 15099-5856 was discovered from Infrared Astronomical Satellite observations (Arendt 1991). IRAS 15099-5856 is only seen at wavelengths longer than  $\sim 10\ \mu\text{m}$  and shows a complicated morphology with a bright central compact source, a surrounding halo of  $\sim 1'$  radius with knots and spurs, and several extended ( $\sim 4'$ ), knotty arc-like filaments (Figure 1; Koo et al. 2011). In MSH 15–52, it is thought that the reverse shock from the

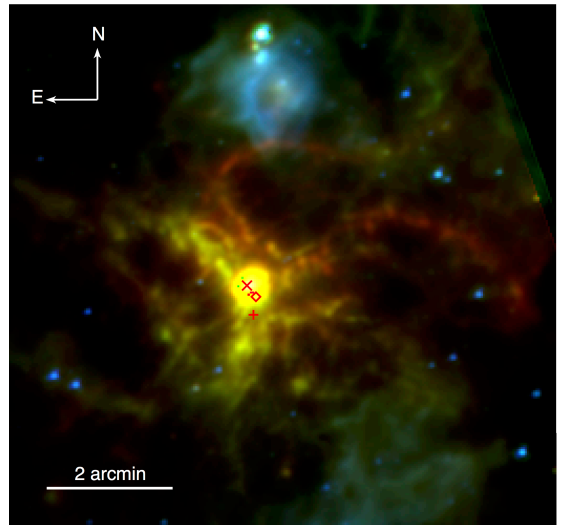


**Figure 1.** Three-color image of IRAS 15099-5856 produced with AKARI S11 (B,  $11\ \mu\text{m}$ ), L15 (G,  $15\ \mu\text{m}$ ), and L24 (R,  $24\ \mu\text{m}$ ) images, which is adopted from Figure 1 of Koo et al. (2011). The cross ( $\times$ ), diamond, and plus ( $+$ ) symbols present the peak position of IRS1 at  $15\ \mu\text{m}$ , O star Muzzio 10, and the pulsar PSR B1509-58, respectively.

surrounding SNR has not yet arrived at the pulsar wind nebula (Gaensler et al. 2002). The distinguishable morphology in IR from other wavelengths further suggests that IRAS 15099-5856 is not heated by the typical mechanism for the dust IR emission in other SNRs, i.e., collisional heating with hot shocked gas, but requires an alternate heating source, e.g., the O star Muzzio 10 (Arendt 1991). Hence, IRAS 15099-5856 is likely “pristine” supernova ejecta material, not processed by a reverse shock. Such pristine dusty ejecta has been found in Cas A as well, although the heating source in this case is the radiative heating from reverse shock (Laming & Temim 2020; Milisavljevic et al. 2024).

Koo et al. (2011) investigated the central compact source (IRS1) of IRAS 15099-5856 with the AKARI MIR imaging observations and the Spitzer IRS spectroscopy. The absence of emission at short ( $\lesssim 10\ \mu\text{m}$ ) wave bands and the extended morphology observed in the AKARI images imply that IRS1 is an extended source likely heated by a nearby O star Muzzio 10 as proposed earlier (Arendt 1991). A unique feature of IRAS 15099-5856 revealed by the Spitzer IRS spectrum is the prominent crystalline silicate dust features (Koo et al. 2011), which has raised an intriguing question about the origin of IRAS 15099-5856 because it is the first and only detection of crystalline silicate associated with SNRs so far. Koo et al. (2011) proposed a scenario that IRS1 is the material from the progenitor of the SNR ejected at its final evolutionary stage based on the Spitzer spec-

trum which is well explained by dust models including Mg-rich crystalline silicates and the proximity among IRS1, Muzzio 10, and the pulsar PSR B1509-58. In this scenario, IRS1 might have survived the SN blast wave as being shielded by Muzzio 10, the former binary companion star of the progenitor. However, the nature of IRAS 15099-5856 and its association with Muzzio 10 and/or the central pulsar are still uncertain.

While the proper motion of Muzzio 10 is known as  $4.9215 \pm 0.0163$  mas yr<sup>-1</sup> with position angle (PA) = 244.2° (measured from north to east) from the Gaia Data Release 3 (Gaia Collaboration et al. 2016, 2023), the proper motion of PSR B1509-58 has only been derived with huge uncertainties. Gaensler et al. (1999) reported one-sigma upper limits on the pulsar’s proper motion: 39 mas yr<sup>-1</sup> in right ascension and 52 mas yr<sup>-1</sup> in declination. Leung (2018) measured the proper motion of  $\mu_\alpha = 2 \pm 12$  mas yr<sup>-1</sup> and  $\mu_\delta = -50 \pm 24$  mas yr<sup>-1</sup>. The proper motion of the pulsar seems to imply that the site of the SN explosion about 1,700 yrs ago was  $>1'$  apart from Muzzio 10, i.e., no association between the SN progenitor and Muzzio 10, but more accurate measurements are required to confirm.

The Gaia Data Release 3 (Gaia Collaboration et al. 2016, 2023) also reports the parallax of  $0.293 \pm 0.016$  mas for Muzzio 10. This corresponds to the distance of  $3.42 \pm 0.187$  kpc and is much closer than the known distance to MSH 15–52. However, the distance of  $5.2 \pm 1.4$  kpc to the SNR is the middle value of the lower and upper limits from the HI observation (Gaensler et al. 1999). Since the upper limit of  $6.6 \pm 1.4$  kpc is just the tangent point at  $-70$  km s<sup>-1</sup>, the lower limit of  $3.8 \pm 0.5$  kpc derived from the velocity ( $= -55$  km s<sup>-1</sup>) of the HI absorption is only a reliable estimate. This distance is also consistent with the distance to the pulsar PSR B1509-58 ( $= 4.2 \pm 0.6$  kpc) derived from the dispersion measure (DM =  $252.5 \pm 0.3$  cm<sup>-3</sup> pc; Cordes & Lazio 2002; Hobbs et al. 2004; Abdo et al. 2010). The association of IRAS 15099-5856 and Muzzio 10 seems fairly plausible (Koo et al. 2011). Although there is no direct evidence to suggest the association of these two sources with MSH 15–52, it seems very unlikely that they are coincidentally located on the same line-of-sight, taking account of the possible similar distances. In this paper, we assume that the three sources are physically related and assume their distance as 3.4 kpc.

In this paper, we investigate IRS1 of IRAS 15099-5856 as a follow-up of Koo et al. (2011). In Section 2, we present the high-resolution MIR imaging observations of IRS1 and examine the spatial morphology of IRS1 in detail. In Section 3, we analyze the Spitzer spectrum of IRS1 using model calculations to derive the elemental

abundance of gas and investigate dust emission. Particularly, we take account of geometry and energy balance to draw a more physically realistic picture of IRS1. In Section 4, we discuss the origin of crystalline silicate in MSH 15–52 and dust formation in SN ejecta. In Section 5, we summarize and conclude our study.

## 2. MID-INFRARED OBSERVATIONS OF IRAS 15099-5856 IRS1

### 2.1. *T-ReCS Observations and Data Reduction*

We observed the central compact source IRS1 of IRAS 15099-5856 using the Thermal-Region Camera Spectrograph (T-ReCS; Telesco et al. 1998; De Buizer & Fisher 2005) attached on the Gemini South telescope (Program ID: GS-2012A-C-4; PI: Onaka, T.) on 2012 May 11 UT. T-ReCS uses a Raytheon  $320 \times 240$  pixel Si:As IBC array, providing a pixel scale of  $0''.089$  pixel<sup>-1</sup> with a field of view of  $28''.8 \times 21''.6$ . We applied the standard chop-nod technique in order to remove time-variable sky background, telescope thermal emission, and the 1/f noise in detector. The chop throw and angle were  $15''$  and  $20^\circ$ , respectively. Images were obtained with the Si-6 ( $\lambda_0 = 12.33$   $\mu\text{m}$ ,  $\Delta\lambda = 1.18$   $\mu\text{m}$ ), [Ne II] ( $\lambda_0 = 12.81$   $\mu\text{m}$ ,  $\Delta\lambda = 0.23$   $\mu\text{m}$ ), [Ne II]cont ( $\lambda_0 = 13.10$   $\mu\text{m}$ ,  $\Delta\lambda = 0.22$   $\mu\text{m}$ ), Qa ( $\lambda_0 = 18.30$   $\mu\text{m}$ ,  $\Delta\lambda = 1.51$   $\mu\text{m}$ ), and Qb ( $\lambda_0 = 24.56$   $\mu\text{m}$ ,  $\Delta\lambda = 1.92$   $\mu\text{m}$ ) filters, among which the Si-6 and [Ne II]cont filters were used to determine the continuum baseline of the [Ne II] image. For flux calibration, we observed standard stars  $\gamma$  Cru and  $\omega$  Lup (HD 139127) from Cohen standards (Cohen et al. 1999) with the same filters. The total exposure time of IRS1 was 300 sec for the Qa filter and 900 sec for the others. The standard stars were observed with the exposure time of 30 sec for all filters.

Data were reduced by using the custom IDL software MEFTTOOLS version 5.0<sup>1</sup>. During the image stacking, bad-frames such as the ones affected by instrumental artifacts have been excluded via visual inspection. Since IRS1 is an extended source, we need to align the images of different filters. In the observed field, the O star Muzzio 10 is the only MIR point source, and it was only visible in the Si-6 image. Therefore, we first used Muzzio 10 for the absolute astrometry of the Si-6 image. Then, we used standard stars observed in the same sequence of filters as IRS1 for correcting the relative astrometry among different-filter images with respect to the Si-6 image. Although this is a rough correction only using one star, the peak position of IRS1 in the Qa-band

<sup>1</sup> MEFTTOOLS was developed and provided by James M. De Buizer via <http://www.jim-debuizer.net/research/>, but it is no longer available.

( $\lambda_0 = 18.30 \mu\text{m}$ ) is coincident with the peak position defined based on the AKARI  $15 \mu\text{m}$  image within  $<0''.2$ . The seeing estimated from the standard stars is about  $0''.6$ . For flux calibration, the standard star  $\omega$  Lup was used for all the filters except Qb that used  $\gamma$  Cru. The in-band fluxes of  $\omega$  Lup in the Si-6, [Ne II], [Ne II]cont, and Qa filters are 11.381, 10.569, 10.162, and 5.172 Jy, respectively, at airmass of 1, similar to the airmass of the IRS1 at the time of observations (1.14–1.4); the in-band flux of  $\gamma$  Cru in the Qb filter is 157.567 Jy at airmass of <sup>12</sup>

## 2.2. Mid-Infrared Morphology

Figure 2 displays the [Ne II], Qa, [Ne II]cont, Si-6, and Qb images of IRS1 obtained with T-ReCS and the AKARI S11 ( $\lambda_0 = 11 \mu\text{m}$ ) image with the contours of Qa (green, black) and [Ne II] (cyan) overlaid. The T-ReCS images were smoothed by a Gaussian kernel with a standard deviation of  $1''$ . In the AKARI image with low spatial resolution, IRS1 is elliptically extended along east-west direction with PA of  $110^\circ$ . It is also extended in the T-ReCS images but shows an irregular morphology with sub structures. In the Qa image, IRS1 consists of two parts in the east and west. The eastern part is extended along northwest-southeast (PA =  $144^\circ$ ) direction and composed of three bright clumps although the brightest peaks are not well defined. The western part, on the other hand, is extended along northeast-southwest (PA =  $50^\circ$ ) direction and composed of a bright compact knot and diffuse emission. The size of the bright knot obtained by Gaussian fitting is about  $2''.7 \times 1''$  in FWHM. Owing to this bright knot, the surface brightness of the western part is comparable to the brightness of the eastern part (see below) although the western part is about half the size of the eastern part. The [Ne II] image is overall similar to the Qa image, but the detailed structure is different. The eastern part in [Ne II] is extended as large as the eastern part of the Qa image, but two bright knots are distinctively shown with the size about  $1''.4 \times 2''.7$  and  $1''.3 \times 1''.7$  in FWHM, both of which are larger than the seeing ( $\sim 0''.6$ ) measured from the standard stars. The western part in [Ne II] is very faint and much smaller than the western part in the Qa image.

A remarkable feature is that the distributions of Qa and [Ne II] emission are not consistent with each other. Although the whole extent is similar, the bright peaks have offsets between the two images as shown by the Qa contours on the [Ne II] image and the [Ne II] contours on the Qa image in Figure 2. This discrepancy does

not likely come from the inaccurate astrometry. The relative distances between the peaks are also different in the two images. The Qa image mostly traces dust distribution since the Qa band covers the wavelengths where the amorphous silicate dust continuum and one of the strong features of crystalline silicate exists (Koo et al. 2011, see also Section 3.1). Therefore, the Qa and [Ne II] images obtained with T-ReCS indicate not only a complex, inhomogeneous morphology of IRS1 itself but also different distributions of the gas and dust in IRS1.

The other T-ReCS images besides Qa and [Ne II] do not show any particular emission. The [Ne II]cont image shows no emission, implying no continuum emission in the [Ne II] image. There is weak continuum around  $13 \mu\text{m}$  in the Spitzer IRS spectrum of IRS1 (see Figure 3), but it may be too weak to be detected in the T-ReCS image. The Si-6 image shows the emission almost identical to [Ne II]. This implies that there is no other line except [Ne II]. While IRS1 is bright at wavelengths longer than  $15 \mu\text{m}$  with the spectral energy distribution (SED) peaking at around  $30 \mu\text{m}$  (see Figure 7), the Qb image at  $24.56 \mu\text{m}$  in Figure 2 does not detect significant emission because of lower sensitivity of the Qb filter. In the Qb image, some faint emission features are shown inside the Qa contours, but they are well below three-sigma ( $3\sigma$ ) where  $\sigma$  ( $\simeq 1.0 \times 10^{-14} \text{ erg s}^{-1} \text{ cm}^{-2}$  for Qb) is an rms noise.

Previously, Koo et al. (2011) suggested that IRS1 is externally heated by Muzio 10, which is  $13''.7$  away from IRS1 to the south, based on the non-detection of an embedded point source in optical/NIR imaging and the temperature of Muzio 10 which is appropriate to produce the observed [Ne II] line luminosity obtained from the Spitzer spectrum (see Section 3 as well). The T-ReCS images also do not show any signature of a point source embedded in IRS1, confirming the previous prediction. A star might be deeply embedded in the bright [Ne II] knots, but non-detection of any stellar source in [Ne II]cont or Si-6 rules out this possibility.

## 2.3. Flux Estimation

We measured the flux of IRS1 from the Qa and [Ne II] images. Applying aperture photometry, we estimated the flux of the whole source, eastern and western parts, and the two bright knots in [Ne II] as listed in Table 1. The source regions were determined by the  $3\sigma$  contours, and the knot regions were determined by the size of the knots. The uncertainty in flux measurements is  $\lesssim 20\%$ . As described earlier, the Qa flux of the western part is smaller than that of the eastern part, but the surface brightness of both are comparable. The [Ne II] flux is concentrated in the bright

<sup>2</sup> <https://webarchive.gemini.edu/20210512-sciops--instruments--michelle/find-band-mid-ir-standard-star-fluxes.html>

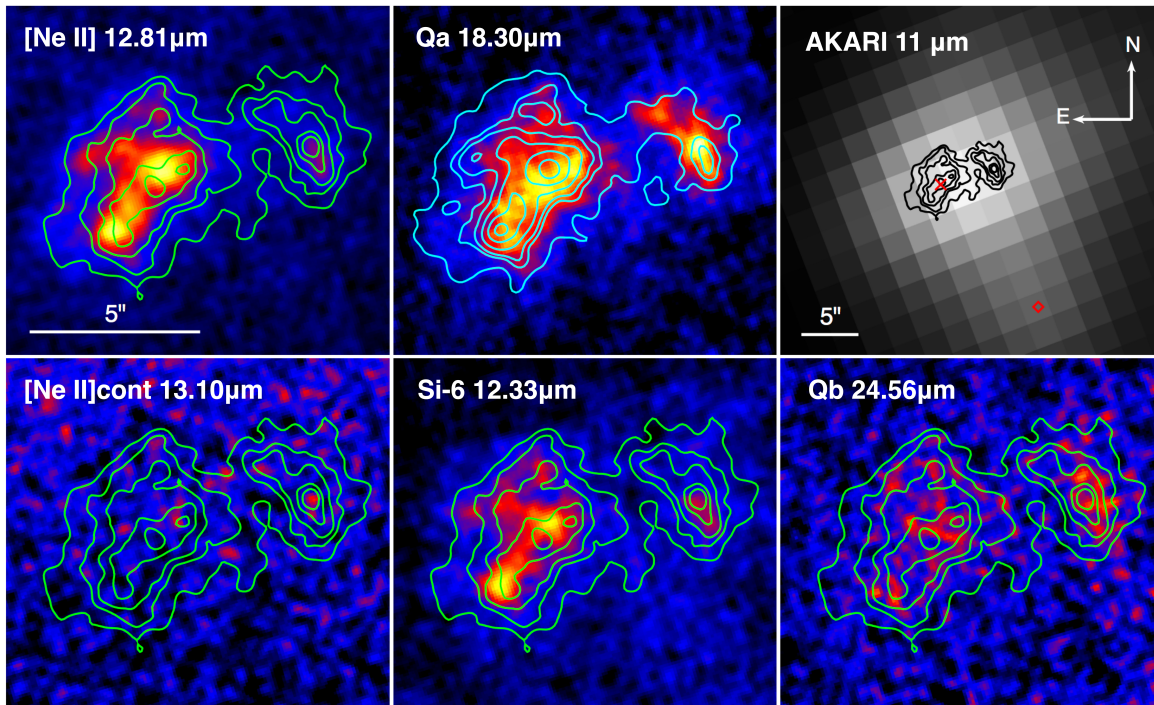


**Figure 2.** T-ReCS images of IRS1 compared with the AKARI S11 ( $11 \mu\text{m}$ ) image. The cyan contours on the Qa image are the  $[\text{Ne II}]$   $12.81 \mu\text{m}$  contours with the flux levels of 0.3, 0.55, 0.65, 0.9, 1.2, and 1.5 mJy from the outermost. The green or black contours on the other images are the Qa  $18.30 \mu\text{m}$  contours with the flux levels of 0.7, 1.1, 1.5, 2.1, and 2.5 mJy. On the AKARI S11 image, the cross and diamond symbols present the peak position of IRS1 at  $15 \mu\text{m}$  and O star Muzzio 10, respectively.

knots. The bright  $[\text{Ne II}]$  knots have surface brightnesses two times larger than that of the eastern region as a whole. We also measured the Si-6 flux for the same source region as  $[\text{Ne II}]$  for comparison. The Si-6 flux is  $1.03 \times 10^{-11} \text{ erg s}^{-1} \text{ cm}^{-2}$ , which is a little larger than the  $[\text{Ne II}]$  flux  $9.58 \times 10^{-12} \text{ erg s}^{-1} \text{ cm}^{-2}$  owing to weak ( $\sim 1 \times 10^{-12} \text{ erg s}^{-1} \text{ cm}^{-2}$ ) continuum at  $11.5\text{--}13 \mu\text{m}$  seen in the Spitzer IRS spectrum (see Section 3.1 and Figure 3).

We compare the flux measured from the T-ReCS images with the flux estimated from the Spitzer IRS spectrum. The Qa flux obtained by using the transmission curve of the Qa filter<sup>3</sup> is 10.16 Jy, larger than the Qa flux from the T-ReCS image by a factor of 1.5. The  $[\text{Ne II}]$  line flux obtained by Gaussian fitting of the emission line (Section 3.1; Table 2) is  $8.21 \times 10^{-12} \text{ erg s}^{-1} \text{ cm}^{-2}$ , about 85% of the  $[\text{Ne II}]$  flux from the T-ReCS image. The flux differences between the T-ReCS and Spitzer observations can be explained by the inhomogeneous morphology of IRS1 and slit-loss correction of the Spitzer IRS spectrum as well as in part by sky chopping op-

eration in the T-ReCS observations. The Spitzer IRS spectrum was obtained with two low-resolution modules: the short-low (SL) module covering  $5.2\text{--}14.5 \mu\text{m}$  and the long-low (LL) module covering  $14.0\text{--}38.0 \mu\text{m}$ . The two slits perpendicularly placed on IRS1 did not cover the same area because of different slit widths (Figure 1 of Koo et al. 2011), and the SL slit along north-south direction with a slit width of  $3''.7$  only partially covered IRS1, requiring slit-loss correction. The slit-loss correction factor was determined by the brightness distribution of the source. IRS1 was assumed as a Gaussian distribution of  $12'' \times 5''$  in size, which is very different from the morphology observed in the Qa and  $[\text{Ne II}]$  images. Since the LL slit width ( $10''.7$ ) is larger than the size of IRS1 estimated in the Qa image, the Spitzer spectrum possibly includes extended, diffuse emission as well that is not detected in the T-ReCS observations, leading to a larger Qa flux from the spectrum. We note that Koo et al. (2011) derived the slit-loss correction factor assuming the two-dimensional brightness distribution of IRS1 given by the AKARI images to match the flux between the AKARI images and Spitzer spectrum, which results in the Qa and  $[\text{Ne II}]$  flux of 14.3 Jy and  $1.2 \times 10^{-11} \text{ erg s}^{-1} \text{ cm}^{-2}$ , respectively.

### 3. CLOUDY MODELING OF THE SPITZER IRS SPECTRUM OF IRS1

<sup>3</sup> <https://webarchive.gemini.edu/20210513-sciops--instruments--treacs/filters.html>

**Table 1.** T-ReCS Qa and [Ne II] Flux of IRS1

Filter	Region	Flux Density	Flux	Area	Brightness
		(Jy)	( $\times 10^{-12}$ erg s $^{-1}$ cm $^{-2}$ )	(arcsec $^2$ )	( $\times 10^{-13}$ erg s $^{-1}$ cm $^{-2}$ arcsec $^{-2}$ )
Qa	whole	6.85	92.6	91.17	10.2
	east	3.84	51.9	29.07	17.9
	west	1.64	22.2	13.51	16.4
[Ne II]	whole	2.28	9.58	71.54	1.34
	east	1.80	7.58	32.57	2.33
	west	0.15	0.63	4.47	1.42
	east knot	0.21	0.87	1.60	5.44
	west knot	0.34	1.45	2.62	5.53

NOTE—The uncertainty in flux measurements is  $\lesssim 20\%$ .

### 3.1. Spectral Characteristics

The Spitzer IRS spectrum of IRS1 presented in Figure 3 was obtained in 2008 October 3 UT (Program ID: 50495; PI: Koo, B.-C.) and examined by Koo et al. (2011). In the AKARI images from N3 ( $\lambda_0 = 3.2 \mu\text{m}$ ) to L24 ( $\lambda_0 = 24 \mu\text{m}$ ), IRS1 is only seen at  $>11 \mu\text{m}$ . In the Spitzer IRS spectrum likewise, continuum emission is extremely weak ( $<0.1$  Jy) at  $\lesssim 13 \mu\text{m}$  and steeply increases to  $\sim 20 \mu\text{m}$ . The most remarkable features in the spectrum are the strong and relatively narrow peaks at 23, 27, and  $34 \mu\text{m}$ , which are well explained by crystalline silicate dust. A model of the IRS spectrum produced by modified-blackbody fitting with dust species including crystalline olivine ( $\text{Mg}_{1.9}\text{Fe}_{0.1}\text{SiO}_4$ ), metal oxides (FeO, MgO), and amorphous silicate fairly well reproduces the observed spectrum, providing total dust mass of  $9 \times 10^{-3} M_\odot$  and dust temperature of  $\sim 55$ – $150$  K at the assumed distance of 4 kpc (see Koo et al. 2011, for details).

The spectrum also shows several ionic emission lines including a strong [Ne II]  $12.81 \mu\text{m}$  line that was partly discussed in Koo et al. (2011). In Figure 3, the emission lines are not clearly seen because of the prominent dust features except the [Ne II] line at  $12.81 \mu\text{m}$ . We detected [Ar III]  $8.99 \mu\text{m}$ , [S IV]  $10.51 \mu\text{m}$ , [Ne II]  $12.81 \mu\text{m}$ , [Ne III]  $15.56 \mu\text{m}$ , [S III]  $18.71 \mu\text{m}$ , and [O IV]/[Fe II]  $25.89/25.99 \mu\text{m}$  lines (Figure 3). We have not detected [Ar II]  $6.99 \mu\text{m}$  line, which is generally much stronger than [Ar III]  $8.99 \mu\text{m}$  line in SNRs, e.g., RCW 103 and Cas A (Oliva et al. 1999; Smith et al. 2009). The non-detection of [Ar II]  $6.99 \mu\text{m}$  line, however, is consistent with our model where the gas is not shock-ionized but photoionized by an O star (see Section 3.4). We also have not detected any hydrogen lines. For the detected lines, we measured the line fluxes by the Gaus-

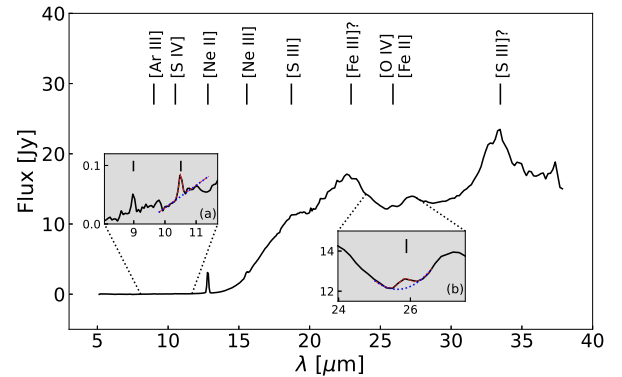


**Figure 3.** Spitzer IRS spectrum of IRS1 (Koo et al. 2011) with the detected lines marked. In the insets, the red dashed and blue dotted lines show the fitted Gaussian curve and baseline, respectively.

sian fitting using the IDL MPFIT package (Markwardt 2009)<sup>4</sup>. The derived line fluxes are listed in Table 2. The flux errors in the table are from the Gaussian fitting and do not include the systematic uncertainty of the observed spectrum. Since the resolving power of the Spitzer IRS LL module<sup>5</sup> between 14 and  $21.3 \mu\text{m}$  is given as  $R = 2.9524\lambda$ , i.e.,  $R \sim 76$  at  $25.9 \mu\text{m}$ , two adjacent lines [O IV]  $25.89 \mu\text{m}$  and [Fe II]  $25.99 \mu\text{m}$  are not resolved. The [S III] line at  $33.48 \mu\text{m}$  also seems to present in the spectrum, but the line flux was not measured because the line is severely blended with the strong dust feature at  $34 \mu\text{m}$ . The FWHM of the emission lines obtained from the Gaussian fitting is from  $0.11$  to  $0.39 \mu\text{m}$

<sup>4</sup> <https://pages.physics.wisc.edu/~craigm/idl/fitting.html>

<sup>5</sup> Spitzer Space Telescope Observer’s Manual version 8.0, Chapter 7.1.6, issued by the Spitzer Science Center (<http://ssc.spitzer.caltech.edu>)

**Table 2.** Detected Emission Lines and their Fluxes from Spitzer IRS Spectrum of IRS1

Line	Wavelength	Flux ( $\times 10^{-12}$ erg s $^{-1}$ cm $^{-2}$ )
	$\mu\text{m}$	
[Ar III]	8.99	0.13( $\pm 0.02$ )
[S IV]	10.51	0.14( $\pm 0.02$ )
[Ne II]	12.81	8.21( $\pm 0.02$ )
[Ne III]	15.56	0.97( $\pm 0.04$ )
[S III]	18.71	0.51( $\pm 0.07$ )
[O IV]/[Fe II] <sup>a</sup>	25.89/25.99	0.93( $\pm 0.07$ )

<sup>a</sup>[O IV] and [Fe II] lines are not resolved at the spectral resolution of the Spitzer IRS LL module.

depending on the wavelength. These line widths are comparable to the spectral resolving power, implying that the velocity of the ionic lines is not resolved.

### 3.2. Emission Line Ratios

The IR fine-structure emission lines are frequently used as a diagnostic tool in the investigations of gaseous nebulae, ionized regions, or obscured clouds. Particularly, the line ratios of some specific lines have a tight correlation, providing physical conditions of the region of interest (Dinerstein 1995; Dopita & Sutherland 2003). In Figure 4, we present the line ratio diagram  $[\text{Ne III}]_{15.56\mu\text{m}}/[\text{Ne II}]_{12.81\mu\text{m}}$  versus  $[\text{S IV}]_{10.51\mu\text{m}}/[\text{S III}]_{18.71\mu\text{m}}$  of various astronomical objects with the observed line ratios of IRS1. The line ratios of the objects except novae were obtained from the literature: H II regions in the Galaxy and Large/Small Magellanic Clouds (LMC/SMC) from Tables 2 and 5 of Giveon et al. (2002); giant H II regions from Table 2 of Lebouteiller et al. (2008); LMC/SMC planetary nebulae (PNe) from Table 2 of Bernard-Salas et al. (2008); a luminous blue variable candidate (cLBV) G79.29+0.46 from Jiménez-Esteban et al. (2010). The line ratios of novae were obtained from the model calculations using the one-dimensional plasma simulation code CLOUDY<sup>6</sup> version C13 (Ferland et al. 2013). CLOUDY solves the ionization, chemical, and thermal state of material exposed to an external radiation field or other heating source, and predicts observable quantities such as emission and absorption spectra that can be compared with observations. The nova models were cal-

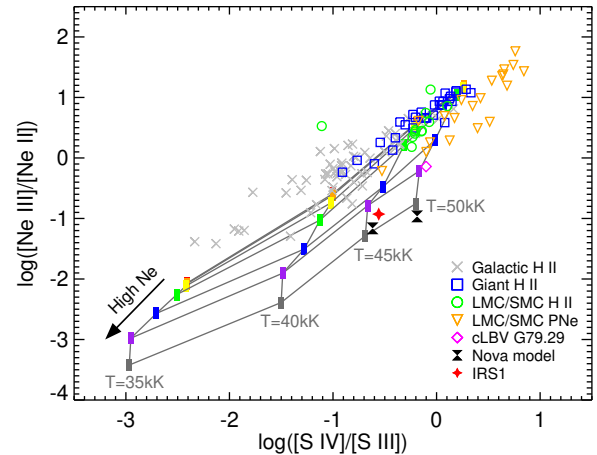


**Figure 4.**  $[\text{Ne III}]_{15.56\mu\text{m}}/[\text{Ne II}]_{12.81\mu\text{m}}$  versus  $[\text{S IV}]_{10.51\mu\text{m}}/[\text{S III}]_{18.71\mu\text{m}}$  line ratio diagram of various astronomical objects (gray cross and open symbols), CLOUDY models of novae (black filled hour glass), and IRAS 15099-5856 IRS1 (red star). The gray lines are the CLOUDY model grid produced with hydrogen density  $n(\text{H})=100$  cm $^{-3}$ , heating source temperature from 35,000 K to 50,000 K, and ISM abundance with varying neon abundance. The small vertical bars in orange, yellow, green, blue, purple, and gray indicate neon abundance from  $-4.0301$  to  $-1.5301$  with an interval of 0.5 in log scale relative to hydrogen.

culated by assuming a blackbody of  $T_{\text{eff}} = 47,000$  K and  $L = 6.3 \times 10^{36}$  erg s $^{-1}$  (Schwarz et al. 2007) and by adopting the abundances of the novae V1500 Cygni (Ferland & Shields 1978) and V838 Her (Schwarz et al. 2007), which show enhanced metal abundances (see Table 3). We also overlay a CLOUDY model grid to examine how the line ratios depend on the physical parameters. The model grid was produced with hydrogen density  $n(\text{H})=100$  cm $^{-3}$ , heating source temperature from 35,000 K to 50,000 K, and the ISM abundance with varying neon abundance from  $-4.0301$  (the ISM abundance) to  $-1.5301$  in log scale relative to hydrogen, i.e.,  $n(\text{Ne})$  from  $9.33 \times 10^{-3}$  cm $^{-3}$  to  $2.95$  cm $^{-3}$ . For the ISM abundance, we adopted the protosolar abundance (Asplund et al. 2009, see also Table 3). The shapes of the radiation fields (SEDs) of heating sources were adopted from the pre-calculated stellar atmospheric models of the Tlusty OB star grids (Lanz & Hubeny 2003, 2007) provided along with the CLOUDY code from which we selected the main-sequence star models at solar metallicity for a given temperature.

It has been known that there is a good correlation between  $[\text{Ne III}]_{15.56\mu\text{m}}/[\text{Ne II}]_{12.81\mu\text{m}}$  and  $[\text{S IV}]_{10.51\mu\text{m}}/[\text{S III}]_{18.71\mu\text{m}}$  (e.g., Martín-Hernández et al. 2002). The relation is almost linear, and it suggests that the two line ratios are almost equally affected by the hardness of the ionizing radiation. In terms of the

<sup>6</sup> <https://www.nublado.org>

stellar  $T_{\text{eff}}$ , the observed line ratios of the H II regions of low to high ionization structures can be described with  $T_{\text{eff}} = 35,000$  K to  $50,000$  K (Figure 4; see also Figure 2 of Martín-Hernández et al. 2002). Figure 4 shows that the relation is in general consistent with the theoretical relation expected for H II regions with the ISM abundance, although the majority of the H II regions with low-ionization structure appears to be above the theoretical line. In contrast, the nova models are located well below the theoretical relation for the ISM abundance, which is likely due to the high abundances of heavy elements. The CLOUDY model grid, for example, demonstrates how the line ratios vary with neon abundance, and it indicates that the enhanced neon abundance lowers the  $[\text{Ne III}]_{15.56\mu\text{m}}/[\text{Ne II}]_{12.81\mu\text{m}}$  ratio. The observed line ratios of IRS1 are similar to those of nova, implying that the elemental composition of IRS1 might be similar to that of nova. Hence, we adopt the nova abundance as an initial abundance set for our modeling of the Spitzer IRS spectrum of IRS1 in Section 3.4.

We note that there is an issue about the line ratios of IRS1 derived from the Spitzer IRS spectrum. As described in Section 2.3, IRS1 was observed with two IRS modules with different slit widths that covered different parts of IRS1. Since the two lines of each pair in Figure 4 ( $[\text{S IV}]$  and  $[\text{S III}]$ ;  $[\text{Ne III}]$  and  $[\text{Ne II}]$ ) are from different modules, their uncertainty can be large depending on the slit-loss correction. We compare the line ratios of IRS1 on the empirical relation  $\log([\text{Ne III}]/[\text{Ne II}]) = 0.81 \times \log([\text{S IV}]/[\text{Ne II}]) + 0.36$  (Groves et al. 2008) which was derived from the archival spectra of a wide range of astrophysical objects from nearby H II regions to ultraluminous infrared galaxies obtained by Spitzer and Infrared Space Observatory (ISO; Kessler et al. 1996). With the  $[\text{S IV}]/[\text{Ne II}]$  ratio derived from the same SL module, the  $[\text{Ne III}]/[\text{Ne II}]$  ratio expected by this relation is 0.09, which is comparable to  $[\text{Ne III}]/[\text{Ne II}] \sim 0.12$  derived from the observed spectrum. Therefore, we assume that the slit-loss correction is acceptable, although there is still uncertainty from the brightness distribution between the one we assumed (i.e., 2D Gaussian distribution) and the real distribution of IRS1.

### 3.3. Model Parameters and Assumptions

Previously, Koo et al. (2011) modeled the Spitzer IRS spectrum as thermal emission from several independent dust components using modified blackbodies. Their models well reproduce the observed spectrum, but the derived dust temperatures show large differences ranging from 55 K to 150 K because they treated dust com-

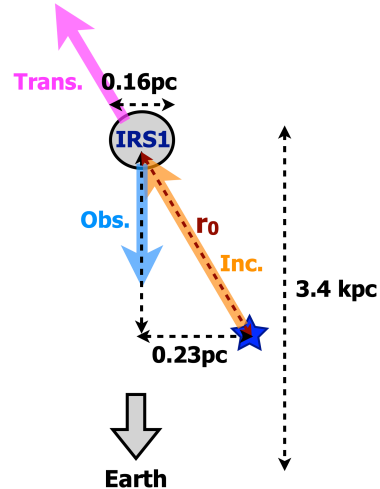


**Figure 5.** Geometry of CLOUDY model calculations of IRS1. The blue star is the heating source Muzzio 10. ‘Inc.’ refers to the incident continuum radiation from Muzzio 10. ‘Obs.’ refers to the emission we observe. This includes the backscattered incident radiation of Muzzio 10 and the radiation emitted by IRS1 itself. ‘Trans.’ refers to the transmitted radiation that includes the attenuated incident radiation of Muzzio 10 and the radiation by IRS1. In the model calculations, the separation between IRS1 and Muzzio 10 ( $r_0$ ) has been fixed as 0.45 pc (See Section 3.4).

ponents independently. In this study, we model the IRS spectrum using CLOUDY to include physical process and energy balance. We first set the geometry of model calculation. The observations imply that IRS1 with a size  $9''.6 \times 5''.1$  (from the AKARI image; Koo et al. 2011) or  $0.16$  pc  $\times$   $0.08$  pc at the distance of 3.4 kpc, is externally heated by Muzzio 10 separated by  $13''.7$  or 0.23 pc, in projected distance. The separation between IRS1 and Muzzio 10 ( $r_0$ ) in principle should be treated as a free parameter because it significantly affects the radiation absorbed by IRS1 and total dust mass, but we fixed it to reduce the number of free parameters based on the initial models (See Section 3.4). We also fixed the thickness of IRS1 as the same as the major axis (0.16 pc) of IRS1 on the projected sky. Figure 5 is a schematic figure of the geometry. Since the heating source (= Muzzio 10) is outside the cloud (= IRS1), we adopted a covering factor (=  $\Omega/4\pi$ , where  $\Omega$  is an area of the cloud divided by the distance between the heating source and cloud.) to take account into a fraction of the radiation field emitted by the heating source that actually strikes the cloud. In Figure 5, ‘Obs.’ is what we observe, which is the emission from the illuminated face of the cloud back into the direction towards the heating source. This includes the backscattered incident radiation of Muzzio 10 and the radiation emitted by IRS1 itself. Meanwhile,



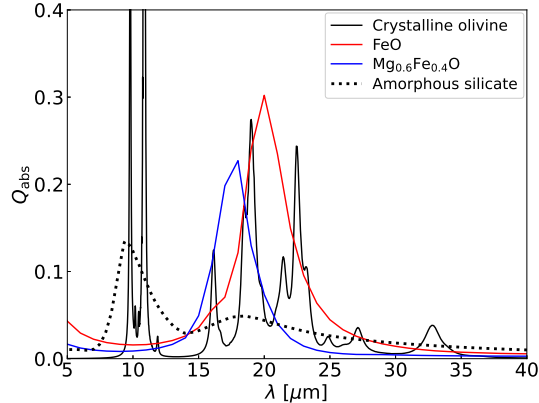


**Figure 6.** Absorption efficiency ( $Q_{\text{abs}}$ ) of dust species used in CLOUDY model calculations. The black, red, and blue solid lines represent crystalline olivine ( $\text{Mg}_{1.9}\text{Fe}_{0.1}\text{SiO}_4$ ), FeO, and  $\text{Mg}_{0.6}\text{Fe}_{0.4}\text{O}$ , respectively. The black dotted line represents amorphous silicate. The size of a dust grain is  $0.1 \mu\text{m}$  in radius except FeO with a radius of  $0.25 \mu\text{m}$ .

the ‘transmitted (Trans.)’ radiation is the net emission emerging from the shielded face of the cloud, which includes the attenuated incident radiation of Muzio 10 and the radiation by IRS1. If the geometry is reversed, i.e., Muzio 10 is behind IRS1, the transmitted radiation would be what we observe, and it will show the attenuated stellar continuum of Muzio 10 in optical and NIR (see Figure 7).

The heating source in model calculations was fixed as Muzio 10. The spectral type of Muzio 10 is O4.5III(fp) (M. Bessell 2010, private communication) or O5n(f)p (Maíz Apellániz et al. 2016). Since the luminosity class is uncertain for the latter, we adopted the stellar parameters of an O4.5III star (Martins et al. 2005):  $T_{\text{eff}} = 40,500 \text{ K}$ ,  $\log g = 3.71 \text{ cm s}^{-2}$ , and  $\log L/L_{\odot} = 5.76$  or  $\log Q_0 = 49.52 \text{ s}^{-1}$ . For the shape of the radiation field, we used the Tlusty O star model at solar metallicity with  $T_{\text{eff}} = 40,000 \text{ K}$  and  $\log g = 3.75 \text{ cm s}^{-2}$  (Lanz & Hubeny 2003).

Dust species were adopted from Koo et al. (2011). We calculated the absorption/scattering coefficients of each dust from their optical constants following the Bohren-Huffman Mie scattering (Bohren & Huffman 1983) and compiled dust opacity files using the grain code in CLOUDY. The optical constants of dust were adopted from the literature: crystalline olivine ( $\text{Mg}_{1.9}\text{Fe}_{0.1}\text{SiO}_4$ ) from Fabian et al. (2001); FeO and  $\text{Mg}_{0.6}\text{Fe}_{0.4}\text{O}$  from Henning et al. (1995). For amorphous silicate, we used the opacity provided in CLOUDY. The compiled opacity assumes a spherical dust grain with a size of  $0.25 \mu\text{m}$  for FeO and  $0.1 \mu\text{m}$  for the others. Figure 6 presents the absorption efficiency ( $Q_{\text{abs}}$ ) of each dust species.

### 3.4. CLOUDY Models of IRS1

With the assumed geometry, heating source of an O4.5III star, and adopted dust species, we modeled IRS1 using CLOUDY to derive its physical and chemical characteristics. Since a large number of free parameters are involved in CLOUDY calculations, we constrained some parameters from the observations. There is no hydrogen line emission detected in the Spitzer spectrum or optical/NIR images. This requires very low hydrogen density, so we have assumed that hydrogen is depleted in IRS1 and fixed the hydrogen density as  $n(\text{H}) \sim 10^{-5} \text{ cm}^{-3}$ . In CLOUDY, the initial abundance can be adopted from the stored abundance sets, e.g., HII regions, general ISM, novae, and PNe. Based on the line ratio diagram (Figure 4, Section 3.2), we adopted the gas-phase abundance of the nova V1500 Cyg listed in the third column of Table 3 but with little hydrogen as an initial gas-phase abundance set and adjusted the amounts of the elements. The elements not listed in Table 3 were not included in the calculations. Grains were included by specifying dust opacity files (Section 3.3).

We first determine the scale factor that is applied to all the metals (the elements heavier than helium) and grains to fit the observed MIR flux level. With the hydrogen density  $\log n(\text{H}) = -4.9$ , we obtained a scale factor of  $10^{7.65}$  relative to hydrogen. We also found that  $r_0 = 0.45 \text{ pc}$  reasonably well fits the observed flux, so we fixed  $r_0$  as  $0.45 \text{ pc}$ . Then, the abundance of each element is further adjusted to match the observed flux. Figure 7 shows the Spitzer IRS spectrum of IRS1 with broadband observations. In the figure, the flux of the Spitzer spectrum is about 30% smaller than the AKARI 11, 15, and  $24 \mu\text{m}$  broadband fluxes because of the assumed profile in the slit-loss correction (Section 2.3). The AKARI fluxes were derived by the aperture photometry with a circle of  $25''$  radius (Koo et al. 2011), so the aperture contains extended diffuse emission, leading to larger fluxes. We fit the CLOUDY model to the flux of the Spitzer spectrum. After roughly fitting the MIR flux level, we searched for a model that reproduces the observed dust features by changing the amount of four dust species: crystalline olivine, FeO,  $\text{Mg}_{0.6}\text{Fe}_{0.4}\text{O}$ , and silicate. With the fixed dust abundance, we then determined the gas abundance that explains the observed line flux derived in Section 3.1 by changing the densities of six elements involved in the formation of the observed emission lines: nitrogen, oxygen, neon, sulphur, argon, and iron. These six ions do not independently act but are tightly correlated to each other. For example, the increased neon abundance does not always lead

**Table 3.** Abundances used in the CLOUDY Modeling

Atom	ISM <sup>a</sup>	Nova (V1500 Cyg) <sup>b</sup>	Nova (V838 Her) <sup>c</sup>	IRS1 Model	
				Gas Phase	Grain
H	1.00E+02	3.16E+07	3.16E+07	1.26E-05	...
He	9.55E+00	3.09E+06	4.47E+06	1.23E-06	...
C	2.95E-02	2.95E+04	6.03E+04	5.29E-01	...
N	7.41E-03 (-0.60)	3.09E+05 (1.02)	7.41E+04 (0.09)	5.51E-04 (-2.98)	...
O	5.37E-02 (0.26)	5.37E+05 (1.26)	2.82E+04 (-0.33)	1.91E+00 (0.56)	6.30E-01
Ne	9.33E-03 (-0.50)	6.46E+04 (0.34)	1.91E+05 (0.50)	3.25E+01 (1.79)	...
Mg	4.37E-03 (-0.83)	1.20E+03 (-1.39)	1.58E+03 (-1.58)	2.14E-02 (-1.39)	1.80E-01
Si	3.55E-03 (-0.92)	1.12E+03 (-1.42)	2.04E+03 (-1.47)	2.00E-02 (-1.42)	1.43E-01
S	1.45E-03 (-1.31)	5.13E+02 (-1.76)	6.92E+03 (-0.94)	9.76E-02 (-0.73)	...
Cl	1.86E-05 (-3.20)	5.89E+00 (-3.70)	5.89E+00 (-4.01)	1.06E-04 (-3.70)	...
Ar	2.75E-04 (-2.03)	1.15E+02 (-2.41)	1.15E+02 (-2.72)	1.86E-01 (-0.45)	...
Fe	3.47E-03 (-0.93)	1.48E+03 (-1.30)	8.51E+03 (-0.85)	1.19E+01 (1.35)	1.64E-01

NOTE— The abundance is the absolute number density ( $\text{cm}^{-3}$ ) applied to the CLOUDY models. All the abundances except IRS1 Model are the gas-phase abundance. The numbers in parentheses are the number density of the element relative to carbon in log scale, which shows the relative abundances among metals.

<sup>a</sup>For ISM, the protosolar abundance (Asplund et al. 2009) is adopted.

<sup>b</sup>The nova abundance stored in CLOUDY derived by Ferland & Shields (1978) for V1500 Cygni.

<sup>c</sup>The nova abundance derived for V838 Her (Schwarz et al. 2007).

to stronger neon lines, or the increased iron abundance strengthens the [Ne II] line as well as iron lines but not the [Ne III] line. Since hydrogen is depleted in IRS1, the heating process mostly depends on photoelectric heating by dust and heavy elements rather than photoionization by hydrogen; thus, changes of the metal and dust abundances affect the heating and cooling processes, complicating the model calculations. With a large number of free parameters and limited observational data, it is improbable to find the only model that perfectly fits IRS1. Instead, we intend to present a reference model that reasonably well explains the observations and to discuss some parameters that affect the modeling results. The final abundances of the reference model in gas phase and those depleted onto grains are presented in the fifth and sixth columns of Table 3. For the gas-phase, we also present the reference metal abundances to carbon rather than hydrogen which is depleted in IRS1 for the comparison between IRS1 and others.

In Figures 7 and 8, we present the reference model of IRS1 in red color that fits fairly well the Spitzer IRS spectrum in both dust features and line intensities. The model was reddened by the column density of  $9.5 \times 10^{21} \text{ cm}^{-2}$  with  $R_V = 3.1$  (Gaensler et al. 2002; Koo et al. 2011). In Figure 7, the red curve presents

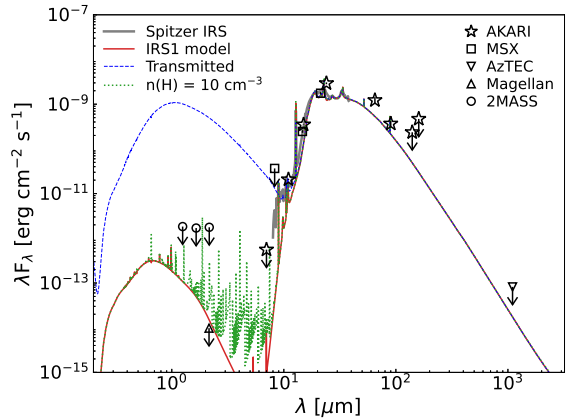


**Figure 7.** SEDs of IRS1 from the observations and CLOUDY models. Open symbols are the broadband fluxes from various observations as labeled in the legend (Koo et al. 2011). The symbols with a down arrow represent upper limits. The red line is the SED of the reference model of IRS1 that is expected to be observed. The blue-dashed line is also the reference model but presents the transmitted emission (Section 3.3). The green-dotted line shows the model with some amount of hydrogen ( $n(\text{H}) = 10 \text{ cm}^{-3}$ ) for the comparison with the reference ( $n(\text{H}) = 10^{-5} \text{ cm}^{-3}$ ). The Spitzer IRS spectrum of IRS1 is also displayed by a thick grey line.

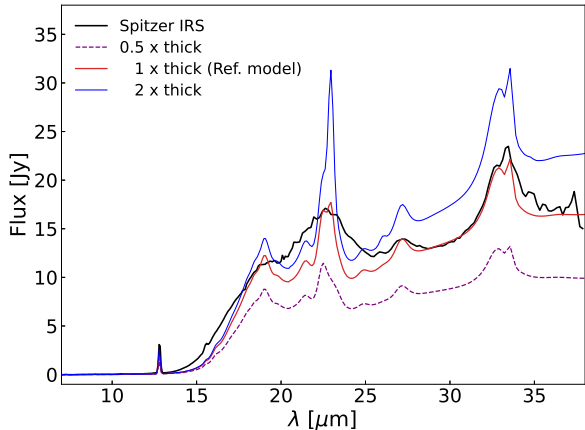


**Figure 8.** Spitzer IRS spectrum (black) of IRS1 and CLOUDY models with different thickness. The red solid line is the reference model that fits fairly well the Spitzer IRS spectrum in both dust features and line intensities. The purple dashed and blue solid lines are the models calculated with the same parameters as the reference model but with a half and twice of the thickness, respectively. The model spectra were smoothed to the spectral resolution of the Spitzer IRS modules.

the SED of the reference model expected to be observed for the assumed geometry (Figure 5). The model SED again confirms that IRS1 is externally heated. If a heating source is embedded in IRS1, we would observe an SED similar to the transmitted emission displayed by a blue-dashed curve in Figure 7 that exhibits strong attenuated incident stellar continuum in optical and NIR. An embedded star with low temperature may suppress the optical/NIR flux, but such temperature is too low to produce the observed [Ne II] line.

In Figure 8, the model spectrum was smoothed to the spectral resolution of the Spitzer IRS modules. The model reproduces the observed dust features at 18, 23, 27, and 34  $\mu\text{m}$  but with narrower width for the 23  $\mu\text{m}$  peak. The continuum slope from 15 to 20  $\mu\text{m}$  in the model is also steeper than observed. These differences can be explained by the sizes and shapes of dust grains. We have assumed a spherical dust grain of 0.1  $\mu\text{m}$  (or 0.25  $\mu\text{m}$  for FeO) because of the limited availability of the optical constants or opacities of dust in MIR, but dust properties in fact highly depend on both dust size and shape (e.g., Koike et al. 1989, 2010; Min 2015). For example, the 10  $\mu\text{m}$  silicate feature becomes broader and is shifted to longer wavelength as the grain shape deviates from a perfect sphere. The prominent features of forsterite (Mg-rich crystalline silicate) are also significantly suppressed for the dust grains with larger size (Figure 5 of Min 2015) or elliptical shape (Figure 9 of Koike et al. 2010). This implies that the model of the

**Table 4.** Dust Parameters of IRS1 from the Reference Model

Component	Mass ( $10^{-3} M_{\odot}$ )	Temperature (K)
Crystalline olivine ( $\text{Mg}_{1.9}\text{Fe}_{0.1}\text{SiO}_4$ )	0.05	79
FeO	0.01	67
$\text{Mg}_{0.6}\text{Fe}_{0.4}\text{O}$	0.21	78
Amorphous silicate	1.74	71
Total	2.02	...

IRS spectrum can be improved by using elliptical and/or larger dust grains. We note that the dust models in Koo et al. (2011) that used a continuous distribution of ellipsoids (CDE) for FeO give a better fit for the steep continuum shape at 15–20  $\mu\text{m}$ , but their models produced by independent dust components result in the temperature of 90–150 K for FeO and  $\text{Mg}_{0.6}\text{Fe}_{0.4}\text{O}$  (or MgO), which is much higher than the temperature of the other dust components around 55 K.

Table 4 presents dust mass and temperature obtained from the reference model. Total dust mass is  $2.02 \times 10^{-3} M_{\odot}$ . The derived dust-to-gas ratio is rather high with 0.02. Most dust mass is contributed by amorphous silicate. The contribution from crystalline olivine is small but indispensable to fit the observed dust features. The total dust mass is  $\sim 31\%$  of the dust mass of  $9 \times 10^{-3} d_4^2 M_{\odot}$  (i.e.,  $6.5 \times 10^{-3} M_{\odot}$  when scaled to  $d = 3.4$  kpc) derived from the modified-blackbody fit (Koo et al. 2011), likely due to the constrained geometry. Total dust mass highly depends on the geometry such as  $r_0$  or the thickness of IRS1 both of which were fixed in our calculations. If we increase  $r_0$ , the dust mass becomes larger. For example, a model with  $r_0 = 0.52$  pc gives more than twice the dust mass of the reference model but with dust temperatures about 12–15 K lower than presented in Table 4. The models with larger  $r_0$  thus tend to predict larger fluxes at long ( $\gtrsim 100 \mu\text{m}$ ) wavelengths and make the SED fits worse in FIR. Comparing to Koo et al. (2011), the relative fraction and temperature of the individual dust species are also different. This may come from the differences in dust opacity. While the optical constants of each dust were adopted from the same literature, the calculations of dust absorption coefficients are different likely due to the assumed shapes and sizes of dust grain, resulting in slightly different dust properties. For example, the strength of two peaks at 18  $\mu\text{m}$  and 23  $\mu\text{m}$  of the absorption coefficient of crystalline olivine are comparable

in our calculations (Figure 6), while the 23  $\mu\text{m}$  peak is only 60% relative to the 18  $\mu\text{m}$  peak in Koo et al. (2011), requiring larger mass and lower temperature to fit the observed 23  $\mu\text{m}$  feature. For FeO, we assume a spherical grain of 0.25  $\mu\text{m}$ , whereas Koo et al. (2011) assumed a CDE with a size of 0.1  $\mu\text{m}$  which shows the weaker, broader, and asymmetric peak of the absorption coefficient.

The CLOUDY model also reproduces several ionic lines observed in the IRS spectrum. In Table 3, the reference model indicates that neon, argon, and iron are enhanced in IRS1. As we pointed out earlier, the reference model is not the only model that can explain IRS1, but the overall trend in abundance should not be very different in order to produce the observed lines. The predicted lines and their fluxes are presented in Table 5 with the relative strength to the observed line fluxes. The predicted line fluxes mostly agree with the observations within  $\lesssim 20\%$  except the  $[\text{S IV}]_{10.51\mu\text{m}}$  and  $[\text{Fe II}]_{25.99\mu\text{m}}$  lines. For the  $[\text{S IV}]_{10.51\mu\text{m}}$  line, the observed line flux could have been overestimated. As seen in the insets of Figure 3, the continuum at 10–11  $\mu\text{m}$  is noisy and shows a discontinuity with a steeper slope compared to the wavelengths  $< 10 \mu\text{m}$ . Considering the predicted line flux of  $[\text{S III}]_{18.71\mu\text{m}}$  well matched to the observation, the overestimation of the line flux of  $[\text{S IV}]_{10.51\mu\text{m}}$  by 10–15% due to a poor baseline is plausible. The flux of the  $[\text{Fe II}]_{25.99\mu\text{m}}$  line could have also been overestimated because the line is located between dust features where the baseline is not reliably defined, but the only 15% of the predicted to observed flux ratio requires another reason besides the overestimation of the observed flux (see below). The CLOUDY model predicts the  $[\text{S III}]$  line at 33.48  $\mu\text{m}$  and  $[\text{Fe III}]$  line at 22.93  $\mu\text{m}$  as well. While these two lines are predicted to be strong, they are blended with the dust features of crystalline olivine at 34  $\mu\text{m}$  and 23  $\mu\text{m}$ , respectively, and so are hardly detectable in the IRS spectrum. In the model spectrum, after we smoothed it to the Spitzer IRS resolution, the  $[\text{S III}]_{33.48\mu\text{m}}$  and the  $[\text{Fe III}]_{22.93\mu\text{m}}$  lines have become hidden under the dust features (Figures 3 and 8).

As pointed out, the  $[\text{Fe II}]_{25.99\mu\text{m}}$  line predicted from the model is much weaker than observed. While we noted that the line detected at  $\sim 25.9 \mu\text{m}$  could be either  $[\text{O IV}]_{25.89\mu\text{m}}$  or  $[\text{Fe II}]_{25.99\mu\text{m}}$ , the CLOUDY model only predicts  $[\text{Fe II}]_{25.99\mu\text{m}}$ . We also believe that  $[\text{Fe II}]$  is more plausible because the UV radiation of an O4.5III star is not hard enough to ionize O III to O IV for which the ionization potential is 54.9 eV. The reason for the weaker  $[\text{Fe II}]$  line in the model is because most iron is in

Fe III or Fe IV as shown in Figure 9 (see also Bautista & Pradhan 1998). The  $[\text{Fe II}]$  line becomes stronger when the thickness of IRS1 increases. In Figure 8 and Table 5, we present two models produced by the same parameters as the reference model except for the cloud thickness: the models with the thickness twice and a half of the thickness of the reference model. In Table 5, the  $[\text{Fe II}]_{25.99\mu\text{m}}$  and  $[\text{Fe III}]_{22.93\mu\text{m}}$  lines are the only lines that significantly vary by thickness. This behavior is also seen in Figure 9 which presents the ionization fraction of neon and iron by depth. In the figure, depth is normalized and is zero at the closest side to the heating source, where the temperature is the highest. The ionization fraction is defined as the number density of each ion of an element among the total number density of the element. Figure 9 shows that the ionization fraction of iron is more sensitive to the thickness compared to neon. For example, all of the neon is in Ne II from the very inside ( $\lesssim 0.15$  of the depth) regardless of the cloud thickness. In contrast, the fraction of iron ions changes through the whole depth depending on the cloud thickness. Therefore, the model of IRS1 could be improved by leaving the cloud thickness as a free parameter or by finding a constraint on the thickness that reproduces the observed  $[\text{Fe II}]_{25.99\mu\text{m}}$  line.

In CLOUDY model calculations, we have assumed the hydrogen density almost zero. We now examine if hydrogen is indeed depleted in IRS1. In Figure 7, we present a model that contains some amount of hydrogen with  $n(\text{H}) = 10 \text{ cm}^{-3}$ . The MIR spectrum of this model is identical to the spectrum of the reference model as long as the total amount of metals and grains are retained the same, but the model with hydrogen shows a group of emission lines from hydrogen in optical and NIR which have not been observed in IRS1. We searched for the  $\text{H}\alpha$  emission around IRS1 from the VST Photometric  $\text{H}\alpha$  Survey of the Southern Galactic Plane and Bulge (VPHAS+; Drew et al. 2014)<sup>7</sup>. The predicted  $\text{H}\alpha$  line flux of the CLOUDY models are  $8.9 \times 10^{-21}$  and  $8.9 \times 10^{-15} \text{ erg s}^{-1} \text{ cm}^{-2}$  for the models with  $n(\text{H}) = 10^{-4.9}$  and  $10 \text{ cm}^{-3}$ , respectively, after applying the extinction by  $N_{\text{H}} = 9.5 \times 10^{21} \text{ cm}^{-2}$  (Gaensler et al. 2002; Koo et al. 2011). For comparison, the  $5\sigma$  limiting magnitude of VPHAS+ is about 20 mag (Drew et al. 2014), or  $1.84 \times 10^{-15} \text{ erg s}^{-1} \text{ cm}^{-2}$  in  $\text{H}\alpha$ . If IRS1 contains hydrogen, even a small amount of  $\lesssim 10 \text{ cm}^{-3}$ , the  $\text{H}\alpha$  emission is expected to be detected in the VPHAS+ images, but no emission has been found around IRS1.

<sup>7</sup> <http://www.vphasplus.org>

**Table 5.** Line Fluxes Predicted from the CLOUDY Models and Relative Intensities to the Observations

Model <sup>a</sup>	[Ar III]	[S IV]	[Ne II]	[Ne III]	[S III]	[Fe III] <sup>b</sup>	[Fe II]	[S III] <sup>b</sup>
(× thick)	8.99 μm	10.51 μm	12.81 μm	15.56 μm	18.71 μm	22.93 μm	25.99 μm	33.48 μm
0.5	1.01E-13 (0.76)	9.35E-14 (0.66)	5.61E-12 (0.68)	7.63E-13 (0.79)	3.43E-13 (0.67)	2.02E-12	5.87E-15 (0.01)	3.73E-12
1.0	1.32E-13 (0.99)	9.83E-14 (0.70)	7.19E-12 (0.88)	7.69E-13 (0.79)	5.75E-13 (1.13)	1.69E-11	1.40E-13 (0.15)	6.82E-12
2.0	1.53E-13 (1.15)	1.00E-13 (0.71)	8.48E-12 (1.03)	7.72E-13 (0.80)	8.93E-13 (1.75)	6.29E-11	1.95E-12 (2.09)	1.22E-11

NOTE—Line flux is in  $\text{erg s}^{-1} \text{cm}^{-2}$  and reddened by the column density  $9.5 \times 10^{21} \text{cm}^{-2}$  with  $R_V = 3.1$  (Koo et al. 2011). The numbers in parentheses are the relative intensities with respect to the observed fluxes.

<sup>a</sup> A scale factor applied to the cloud thickness.

<sup>b</sup> Not seen in the Spitzer IRS spectrum, but likely blended with dust features.

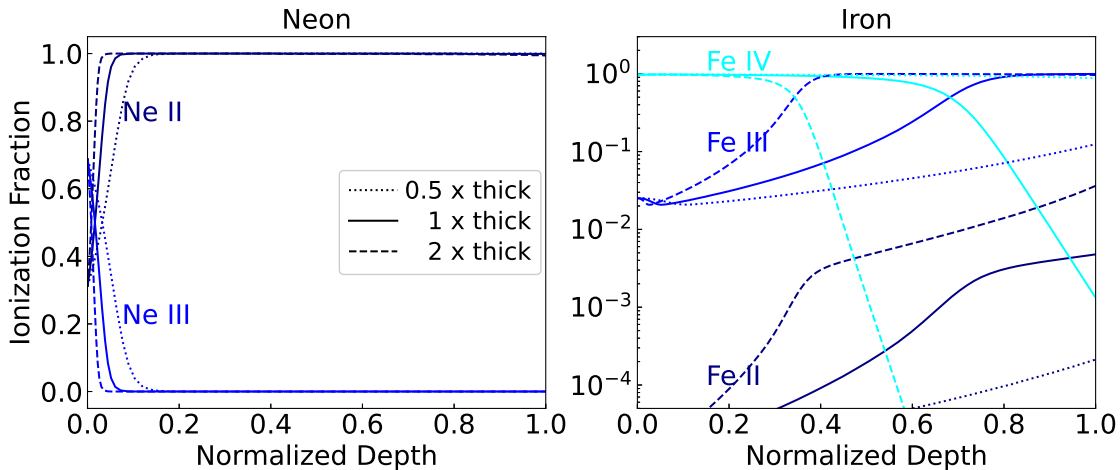


**Figure 9.** Ionization fraction of neon (left) and iron (right) from the CLOUDY models of IRS1, which is defined as the number density of each ion of an element among the total number density of the element. The solid lines are the reference model; the dashed and dotted lines are the models with twice and a half of the thickness, respectively. Ions are presented by different colors: navy (Ne II, Fe II), blue (Ne III, Fe III), and cyan (Fe IV).

This supports our assumption that hydrogen is depleted in IRS1.

#### 4. CRYSTALLINE SILICATE IN MSH 15–52

MSH 15–52 is the first SNR in which crystalline silicate is observed. Our analysis in this paper indicates that the elemental abundance of the IR compact source IRS1 where crystalline silicate has been detected is close to that of SN ejecta with depleted hydrogen and high abundance of metals, particularly neon, argon, and iron. This implies that IRS1 (and probably IRAS 15099-5856 as well) originates from the SN ejecta rather than the mass loss of the SN progenitor as has been proposed by Koo et al. (2011). If this is true, MSH 15–52, besides the existence of crystalline silicate, is a unique object where we can directly observe dust newly formed in the ejecta of SNe Ib/c. Observing the pristine SN dust which has not yet been processed by the SN reverse shock is

also very rare only with a few other cases of G54.1+0.3 (Temim et al. 2017) and Cas A (Sibthorpe et al. 2010; De Looze et al. 2017). While FIR observations (e.g., AKARI, Herschel, and ISO) have revealed cold dust inside SNRs, the spatial resolutions are not high enough to disentangle the SN dust from the surrounding ISM dust and examine dust properties in detail (e.g., Sibthorpe et al. 2010; Koo et al. 2016; Chawner et al. 2020; Millard et al. 2021; Rho et al. 2023, and references therein). The cold and warm dust has been detected in MSH 15–52 as well. Millard et al. (2021) estimated  $0.03\text{--}0.06 M_{\odot}$  of warm (46–52 K) and  $4\text{--}15 M_{\odot}$  of cold (17–20 K) dust, assuming the distance of 5.2 kpc to MSH 15–52, from the two-component blackbody model fitting of the MIR to FIR spectrum obtained by the Long Wavelength Spectrometer (LWS) on board the ISO. Since their spectrum is not background-subtracted, they suggest that the warm and cold dust originate from the SN ejecta

and background ISM, respectively. The dust mass of 0.03–0.06  $M_{\odot}$  at 5.2 kpc is scaled to 0.013–0.026  $M_{\odot}$  at 3.4 kpc. This is several to ten times larger than our results, but a direct comparison of the two dust masses is inappropriate because the LWS spectrum of MSH 15–52 with a large beam size of  $\sim 80''$  (Gry et al. 2003) includes not only IRS1 but the surrounding, diffuse emission.

Dust formation in the SN ejecta of Type II SNe (SNe II) has been widely studied by theoretical calculations (e.g., Sarangi & Cherchneff 2013, 2015; Brooker et al. 2022) as well as the observations of young SNRs, e.g., Cas A (De Looze et al. 2017), SN 1987A (Matsuura et al. 2015), G54.1+0.3 (Rho et al. 2018), and the Crab Nebula (Gomez et al. 2012). In contrast, few studies thus far have been carried out for dust condensation in the ejecta of SNe Ib/c. Observational signatures of dust formation in the SN Ib/c ejecta have been discovered only for a few SNe in the nebula phase: SN Ib 1990I (Elmhamdi et al. 2004), SN Ib(n) 2006jc (Di Carlo et al. 2008; Smith et al. 2008), SN Ic 2020oi (Rho et al. 2021), and SN Ic 2021krf (Ravi et al. 2023). The molecules which become dust seeds in the SN ejecta and their chemical reactions would not be very different between SNe II and Ib/c, but the environments in which dust condensation occurs would differ depending on SN types and progenitor stars. For example, even in the same SN type of IIP, the amount of dust formed in the ejecta and the degree of grain growth predicted by dust condensation models highly depend on the conditions of SN explosion such as progenitor mass, explosion energy, mass of  $^{56}\text{Ni}$ , or clumpy structure of ejecta (Sarangi & Cherchneff 2013, 2015; Brooker et al. 2022). In the ejecta of SNe IIP, dust starts to form a few hundreds days after SN explosion (Sarangi et al. 2018, and references therein). The observations of dust signatures in the SN Ib/c ejecta listed above indicate that the onset of dust formation occurs only 50–70 days after explosion (Di Carlo et al. 2008; Smith et al. 2008; Rho et al. 2021; Ravi et al. 2023), with the exception of SN 1990I ( $\sim 230$  days; Elmhamdi et al. 2004). The reason for the early dust condensation in the ejecta of SNe Ib/c is thought to be due to the rapid decrease in the gas temperature (Nozawa et al. 2008). For SNe Ib/c, the ejected masses are smaller and the expansion velocities are higher than SNe II because the SN Ib/c progenitors have lost most of the hydrogen/helium envelopes before explosion. This leads to a lower density of gas in the ejecta, and gas temperature drops down more quickly than those in typical SNe II. Nozawa et al. (2008) calculated dust formation in the SN 2006jc applying the SN Ib model of a relatively low-mass (6.9  $M_{\odot}$ ) helium star progenitor with an ejecta mass of 4.9  $M_{\odot}$ . Their calculation predicts the gas temperature

reaching a typical dust condensation temperature ranges of 1,000–2,000 K between 50 and 200 days after the SN explosion, which means that dust forms much closer to the explosion center in the ejecta of SNe Ib/c than in the SNe II ejecta (Figure 1 of Nozawa et al. 2008). A similar process of dust formation might have occurred in MSH 15–52 of which progenitor is also speculated as a low-mass helium star.

The different environmental conditions may bring distinctive characteristics of dust formed in the SN Ib/c ejecta, for example, the formation of crystalline silicate or crystallization of amorphous silicate. If silicates are formed at high ( $>1,000$  K) temperature, the crystalline lattice structure is the most favorable state (Molster & Kemper 2005). In a clumpy ejecta, stoichiometric silicate ( $\text{Mg}_2\text{SiO}_4$ ) is predicted to be formed at high densities (Sarangi & Cherchneff 2015). Therefore, the condensation of crystalline silicates could take place in the SN ejecta. Alternatively, silicates first formed in amorphous structure could be crystallized if there is a high-energy process such as heating by pulsar wind nebula, although the condensation temperature and condensing phase of dust are not simply determined but associated with several factors such as gas pressure or gas kinematics (Nagahara et al. 2009; Gail et al. 2013). Then, assuming that crystalline silicates can form in SN dust, why have crystalline silicates not been found in other SNRs except MSH 15–52? This is probably because it is difficult to observe unshocked SN dust without a heating source such as Muzzio 10. Crystalline silicates, even if present, can be undetected in FIR because they exhibit very weak or no spectral signatures at wavelengths longer than 40  $\mu\text{m}$  except for the 69  $\mu\text{m}$  feature (Koike et al. 2003; Sturm et al. 2013). We note that G54.1+0.3 is another SNR of which unshocked SN dust has been revealed by stellar sources (Temim et al. 2017). In G54.1+0.3, the newly formed dust is heated by massive stars in the SNR which are thought to be the members of the same cluster with the SN progenitor. While at least 0.3  $M_{\odot}$  of dust has been found in G54.1+0.3, crystalline silicate dust has not been detected. However, G54.1+0.3 is the remnant of an SN IIP, and the environment of dust condensation would be different from that of MSH 15–52.

While our results suggest a possibility that the crystalline silicate of IRS1 originates from the SN ejecta, the current observational data with limited spatial and spectral resolution can neither confirm the ejecta origin nor rule out the progenitor origin. The Gemini/T-ReCS images show a slightly different spatial distribution between [Ne II] 12.81  $\mu\text{m}$  and Qa 18.30  $\mu\text{m}$  on a spatial scale less than one arcsecond (Figure 2). This is likely

because the [Ne II] line does not trace the Mg-silicate but dust with a very smooth spectrum such as  $\text{Al}_2\text{O}_3$  (Arendt et al. 2014). The spatial distributions of various ionic lines will be required to examine a correlation between the gas and dust features associated with crystalline silicate. The Spitzer IRS spectrum of IRS1 did not resolve the velocity of the gas component. Previously, Koo et al. (2011) favored the progenitor origin of IRS1 based on the low ( $-160 \pm 560 \text{ km s}^{-1}$ ) central velocity of the [Ne II] line. The velocities of the other lines except [Fe II]  $25.99 \mu\text{m}$  are similarly a few hundreds  $\text{km s}^{-1}$  with an average of  $-444 \text{ km s}^{-1}$ , but the uncertainties are huge, as for [Ne II]. The [Fe II] line exceptionally shows a large velocity of  $-1710 \pm 280 \text{ km s}^{-1}$ . This may imply a different origin of [Fe II] from the other lines, but it can be due to an inaccurate measurement of the velocity since the [Fe II] line is weak and embedded between strong dust features (Figure 3).

To confirm the origin of the crystalline silicate in MSH 15–52 and explore the possibility of the formation of crystalline silicates in SN ejecta, further observations as well as theoretical investigations are required. Particularly, it is crucial to examine the spatial distributions of gas and dust in IRAS 15099-5856 through the MIR observations with high resolution and sensitivity (e.g., JWST/MIRI). If the origin of the crystalline silicate is found to be the SN ejecta, MSH 15–52 will give an unprecedented opportunity to investigate dust formation in SN ejecta, which is not yet clearly known.

## 5. SUMMARY AND CONCLUSION

We have presented the MIR imaging observations and analysis of the compact IR source IRS1 of IRAS 15099-5856 in the SNR MSH 15–52, which is the first and only object with crystalline silicate dust associated with SNRs so far. The MIR images obtained by using Gemini/T-ReCS revealed the morphology of IRS1 and spatial distributions of gas and dust at a spatial resolution of  $\lesssim 1''$ . We have also presented the analysis of the Spitzer IRS spectrum of IRS1 that was previously investigated with the models of thermal emission from multiple independent dust components (Koo et al. 2011). In this paper, we have analyzed the ionic lines and modeled the spectrum considering the geometry and energy balance to derive the chemical abundance of gas as well as dust parameters. The derived abundance is close to that of SN ejecta with poor hydrogen and enhanced metals. This suggests the ejecta origin for the crystalline silicate and may imply the possibility of the formation of crystalline silicate in SN ejecta, but the current observational data are still limited in spatial and spectral resolution. If the origin of the crystalline sili-

cate in IRAS 15099-5856 is confirmed as the SN ejecta by future observations, MSH 15–52 will be a unique, invaluable object that proves the formation of crystalline silicate in SN ejecta and where we can directly observe newly-formed dust in the ejecta of SNe Ib/c. In the following, we summarize our main results.

1. The Gemini/T-ReCS images show a complicated, extended morphology of IRS1 with bright clumps and diffuse emission in [Ne II]  $12.81 \mu\text{m}$  and Qa  $18.30 \mu\text{m}$ . The [Ne II]cont image with no emission and the Si-6 image with the almost same emission as [Ne II] indicate that there is no other line or strong continuum emission. The T-ReCS images confirm the previous prediction (Koo et al. 2011) that IRS1 is extended and externally heated by the nearby O star Muzzio 10. We estimated the [Ne II] and Qa flux of IRS1 from the T-ReCS images and compared them with the flux derived from the Spitzer IRS spectrum.
2. The Spitzer spectrum of IRS1 shows prominent dust features at 23, 27, and  $34 \mu\text{m}$  that can be explained by crystalline silicate dust. We also detected several ionic lines of [Ar III]  $8.99 \mu\text{m}$ , [S IV]  $10.51 \mu\text{m}$ , [Ne II]  $12.81 \mu\text{m}$ , [Ne III]  $15.56 \mu\text{m}$ , [S III]  $18.71 \mu\text{m}$ , and [O IV]  $25.89/\text{[Fe II]} 25.99 \mu\text{m}$ . The [O IV] and [Fe II] are not resolved at the spectral resolving power of the Spitzer IRS LL module, but it is likely [Fe II]. The estimated line flux is from 0.13 to  $8.21 \times 10^{-12} \text{ erg s}^{-1} \text{ cm}^{-2}$ . The line widths are comparable to the spectral resolving power, i.e., the velocity is not resolved.
3. We compared the line ratios of  $[\text{Ne III}]_{15.56\mu\text{m}}/[\text{Ne II}]_{12.81\mu\text{m}}$  versus  $[\text{S IV}]_{10.51\mu\text{m}}/[\text{S III}]_{18.71\mu\text{m}}$  of various astronomical objects with the observed line ratios of IRS1 on a model grid generated by CLOUDY (Ferland et al. 2013). The line ratio diagram shows that the abundance of IRS1 is rather close to the nova abundance with enhanced neon. The absence of hydrogen lines in the Spitzer spectrum further suggests that hydrogen is depleted in IRS1.
4. We modeled the Spitzer spectrum of IRS1 using the photoionization code CLOUDY (Ferland et al. 2013). We assumed the cloud IRS1 externally heated by an O4.5III star (Muzzio 10) separated by 0.45 pc. For the gas, the nova abundance was initially adopted but with hydrogen depleted. For the dust species, crystalline olivine ( $\text{Mg}_{1.9}\text{Fe}_{0.1}\text{SiO}_4$ ), FeO,  $\text{Mg}_{0.6}\text{Fe}_{0.4}\text{O}$ , and amorphous silicate were included. Spherical dust grains of  $0.25 \mu\text{m}$  (FeO) and  $0.1 \mu\text{m}$  (the others) were

assumed. We first fitted the dust features and adjusted the abundance of nitrogen, oxygen, neon, sulphur, argon, and iron to find a model that reproduces the observed lines. We have derived a reference model that fairly well fits the Spitzer spectrum and discussed the factors that affect the models.

5. The reference model fits the dust features at 27 and 34  $\mu\text{m}$ , while it does not well fit the 23  $\mu\text{m}$  feature and steeply-increasing continuum between 15 and 20  $\mu\text{m}$ . The derived dust mass is  $2.02 \times 10^{-3} M_{\odot}$  in total, mostly contributed by amorphous silicate. The dust temperature is between 67 and 79 K. The total dust mass is about 31% of the mass previously derived by multi-component blackbody fitting (Koo et al. 2011), but the dust mass depends on the separation to the heating source which was fixed in our modeling. The reference model predicts the emission lines with comparable intensities to the observation except the [S IV] 10.51 $\mu\text{m}$  and [Fe II] 25.99  $\mu\text{m}$  lines. The difference in [S IV]<sub>10.51 $\mu\text{m}$</sub>  is likely due to the overestimation of the observed line flux. On the other hand, [Fe II]<sub>25.99 $\mu\text{m}$</sub>  is predicted much weaker (15%) than the observed intensity. This can be due to the overestimated flux of the observed line in part, but we have also found that the ionization fraction of iron is sensitive to the cloud thickness which was also fixed in our modeling. The model can be improved by changing dust properties (shape or size) and geometrical parameters (e.g. cloud thickness or the separation between IRS1 and Muzio 10), although it is beyond the scope of this paper.
6. The CLOUDY modeling of the Spitzer spectrum indicates that the elemental abundance of IRS1 is close to that of SN ejecta with depleted hydrogen and high abundance of metals, particularly neon, argon, and iron. This implies that IRS1 (and IRAS 15099-5856) is the SN ejecta and that crystalline silicate can form in SN ejecta. To confirm this, further observations to resolve the spatial distri-

butions of various ionic lines, dust continuum, and crystalline silicate will be required.

This work is based in part on observations obtained at the international Gemini Observatory, a program of NSF's NOIRLab, which is managed by the Association of Universities for Research in Astronomy (AURA) under a cooperative agreement with the National Science Foundation on behalf of the Gemini Observatory partnership: the National Science Foundation (United States), National Research Council (Canada), Agencia Nacional de Investigación y Desarrollo (Chile), Ministerio de Ciencia, Tecnología e Innovación (Argentina), Ministério da Ciência, Tecnologia, Inovações e Comunicações (Brazil), and Korea Astronomy and Space Science Institute (Republic of Korea). The Gemini program identification number associated with the data is GS-2012A-C-4. This work is based in part on observations made with the Spitzer Space Telescope, which was operated by the Jet Propulsion Laboratory, California Institute of Technology under a contract with NASA. This work has made use of data from the European Space Agency (ESA) mission *Gaia* (<https://www.cosmos.esa.int/gaia>), processed by the *Gaia* Data Processing and Analysis Consortium (DPAC, <https://www.cosmos.esa.int/web/gaia/dpac/consortium>). Funding for the DPAC has been provided by national institutions, in particular the institutions participating in the *Gaia* Multilateral Agreement. This research of H.-J. K. was supported by Basic Science Research Program through the National Research Foundation of Korea (NRF) funded by the Ministry of Education (RS-2023-00246733). This research of B.-C. K. was supported by the Basic Science Research Program through the National Research Foundation of Korea (NRF) funded by the Ministry of Science, ICT and Future Planning (2020R1A2B5B01001994, RS-2023-00277370). T.O. is supported by the Japan Society for the Promotion of Science (JSPS) KAKENHI Grant Numbers JP 23K22532 and 24K07087.

*Facilities:* Gemini:South (T-ReCS), Spitzer (IRS)

*Software:* CLOUDY version C13 (Ferland et al. 2013), MPFIT (Markwardt 2009)

## REFERENCES

- Abdo, A. A., Ackermann, M., Ajello, M., et al. 2010, ApJ, 714, 927. doi:10.1088/0004-637X/714/1/927
- Andersen, M., Rho, J., Reach, W. T., et al. 2011, ApJ, 742, 7. doi:10.1088/0004-637X/742/1/7
- Arendt, R. G. 1991, AJ, 101, 2160. doi:10.1086/115838
- Arendt, R. G., Dwek, E., Kober, G., et al. 2014, ApJ, 786, 55. doi:10.1088/0004-637X/786/1/55
- Asplund, M., Grevesse, N., Sauval, A. J., et al. 2009, ARA&A, 47, 481. doi:10.1146/annurev.astro.46.060407.145222



- Bautista, M. A. & Pradhan, A. K. 1998, *ApJ*, 492, 650. doi:10.1086/305061
- Bernard-Salas, J., Pottasch, S. R., Gutenkunst, S., et al. 2008, *ApJ*, 672, 274. doi:10.1086/523294
- Bohren, C. F. & Huffman, D. R. 1983, New York: Wiley, 1983
- Brooker, E. S., Stangl, S. M., Mauney, C. M., et al. 2022, *ApJ*, 931, 85. doi:10.3847/1538-4357/ac57c3
- Chawner, H., Gomez, H. L., Matsuura, M., et al. 2020, *MNRAS*, 493, 2706. doi:10.1093/mnras/staa221
- Cohen, M., Walker, R. G., Carter, B., et al. 1999, *AJ*, 117, 1864. doi:10.1086/300813
- Cordes, J. M. & Lazio, T. J. W. 2002, astro-ph/0207156. doi:10.48550/arXiv.astro-ph/0207156
- De Buizer, J. & Fisher, R. 2005, *High Resolution Infrared Spectroscopy in Astronomy*, 84. doi:10.1007/10995082\_12
- De Looze, I., Barlow, M. J., Swinyard, B. M., et al. 2017, *MNRAS*, 465, 3309. doi:10.1093/mnras/stw2837
- Di Carlo, E., Corsi, C., Arkharov, A. A., et al. 2008, *ApJ*, 684, 471. doi:10.1086/590051
- Dinerstein, H. 1995, *The Analysis of Emission Lines: A Meeting in Honor of the 70th Birthdays of D. E. Osterbrock & M. J. Seaton*, 134
- Dopita, M. A. & Sutherland, R. S. 2003, *Astrophysics of the diffuse universe*, Berlin, New York: Springer, 2003. *Astronomy and astrophysics library*, ISBN 3540433627. doi:10.1007/978-3-662-05866-4
- Do-Duy, T., Wright, C. M., Fujiyoshi, T., et al. 2020, *MNRAS*, 493, 4463. doi:10.1093/mnras/staa396
- Drew, J. E., Gonzalez-Solares, E., Greimel, R., et al. 2014, *MNRAS*, 440, 2036. doi:10.1093/mnras/stu394
- Elmhamdi, A., Danziger, I. J., Cappellaro, E., et al. 2004, *A&A*, 426, 963. doi:10.1051/0004-6361:20041318
- Fabian, D., Henning, T., Jäger, C., et al. 2001, *A&A*, 378, 228. doi:10.1051/0004-6361:20011196
- Ferland, G. J., Porter, R. L., van Hoof, P. A. M., et al. 2013, *RMxAA*, 49, 137. doi:10.48550/arXiv.1302.4485
- Ferland, G. J. & Shields, G. A. 1978, *ApJ*, 226, 172. doi:10.1086/156597
- Gaensler, B. M., Brazier, K. T. S., Manchester, R. N., et al. 1999, *MNRAS*, 305, 724. doi:10.1046/j.1365-8711.1999.02500.x
- Gaensler, B. M., Arons, J., Kaspi, V. M., et al. 2002, *ApJ*, 569, 878. doi:10.1086/339354
- Gaia Collaboration, Prusti, T., de Bruijne, J. H. J., et al. 2016, *A&A*, 595, A1. doi:10.1051/0004-6361/201629272
- Gaia Collaboration, Vallenari, A., Brown, A. G. A., et al. 2023, *A&A*, 674, A1. doi:10.1051/0004-6361/202243940
- Gail, H.-P., Wetzel, S., Pucci, A., et al. 2013, *A&A*, 555, A119. doi:10.1051/0004-6361/201321807
- Giveon, U., Sternberg, A., Lutz, D., et al. 2002, *ApJ*, 566, 880. doi:10.1086/338125
- Gomez, H. L., Krause, O., Barlow, M. J., et al. 2012, *ApJ*, 760, 96. doi:10.1088/0004-637X/760/1/96
- Gordon, K. D., Clayton, G. C., Declair, M., et al. 2023, *ApJ*, 950, 86. doi:10.3847/1538-4357/acb59
- Groves, B., Nefs, B., & Brandl, B. 2008, *MNRAS*, 391, L113. doi:10.1111/j.1745-3933.2008.00568.x
- Gry, C., Swinyard, B., Harwood, A., et al. 2003, *The ISO Handbook*, Volume III - LWS - The Long Wavelength Spectrometer Version 2.1 (June, 2003). Series edited by T.G. Mueller, J.A.D.L. Blommaert, and P. Garcia-Lario. ESA SP-1262, ISBN No. 92-9092-968-5, ISSN 0379-6566. European Space Agency, 2003.
- Henning, T., Begemann, B., Mutschke, H., et al. 1995, *A&AS*, 112, 143
- Hobbs, G., Faulkner, A., Stairs, I. H., et al. 2004, *MNRAS*, 352, 1439. doi:10.1111/j.1365-2966.2004.08042.x
- Jiménez-Esteban, F. M., Rizzo, J. R., & Palau, A. 2010, *ApJ*, 713, 429. doi:10.1088/0004-637X/713/1/429
- Kemper, F., Markwick, A. J., & Woods, P. M. 2011, *MNRAS*, 413, 1192. doi:10.1111/j.1365-2966.2011.18204.x
- Kemper, F., Vriend, W. J., & Tielens, A. G. G. M. 2004, *ApJ*, 609, 826. doi:10.1086/421339
- Kessler, M. F., Steinz, J. A., Anderegg, M. E., et al. 1996, *A&A*, 315, L27
- Koike, C., Chihara, H., Tsuchiyama, A., et al. 2003, *A&A*, 399, 1101. doi:10.1051/0004-6361:20021831
- Koike, C., Imai, Y., Chihara, H., et al. 2010, *ApJ*, 709, 983. doi:10.1088/0004-637X/709/2/983
- Koike, C., Komatuzaki, T., Hasegawa, H., et al. 1989, *MNRAS*, 239, 127. doi:10.1093/mnras/239.1.127
- Koo, B.-C., McKee, C. F., Suh, K.-W., et al. 2011, *ApJ*, 732, 6. doi:10.1088/0004-637X/732/1/6
- Koo, B.-C., Lee, J.-J., Jeong, I.-G., et al. 2016, *ApJ*, 821, 20. doi:10.3847/0004-637X/821/1/20
- Kotak, R., Meikle, W. P. S., Farrah, D., et al. 2009, *ApJ*, 704, 306. doi:10.1088/0004-637X/704/1/306
- Laming, J. M. & Temim, T. 2020, *ApJ*, 904, 115. doi:10.3847/1538-4357/abc1e5
- Lanz, T. & Hubeny, I. 2003, *ApJS*, 146, 417. doi:10.1086/374373
- Lanz, T. & Hubeny, I. 2007, *ApJS*, 169, 83. doi:10.1086/511270
- Lebouteiller, V., Bernard-Salas, J., Brandl, B., et al. 2008, *ApJ*, 680, 398. doi:10.1086/587503
- Leung, W.-Y. 2018, Ph.D. Thesis, *High-resolution Radio Study of the Pulsar Wind Nebula MSH 15-52*, The University of Hong Kong, Pokfulam, Hong Kong

- Maaskant, K. M., de Vries, B. L., Min, M., et al. 2015, *A&A*, 574, A140. doi:10.1051/0004-6361/201423770
- Malfait, K., Waelkens, C., Bouwman, J., et al. 1999, *A&A*, 345, 181
- Martín-Hernández, N. L., Vermeij, R., Tielens, A. G. G. M., et al. 2002, *A&A*, 389, 286. doi:10.1051/0004-6361:20020528
- Maíz Apellániz, J., Sota, A., Arias, J. I., et al. 2016, *ApJS*, 224, 4. doi:10.3847/0067-0049/224/1/4
- Markwardt, C. B. 2009, *Astronomical Data Analysis Software and Systems XVIII*, 411, 251. doi:10.48550/arXiv.0902.2850
- Martins, F., Schaerer, D., & Hillier, D. J. 2005, *A&A*, 436, 1049. doi:10.1051/0004-6361:20042386
- Matsuura, M., Dwek, E., Barlow, M. J., et al. 2015, *ApJ*, 800, 50. doi:10.1088/0004-637X/800/1/50
- Matsuura, M., Dwek, E., Meixner, M., et al. 2011, *Science*, 333, 1258. doi:10.1126/science.1205983
- Milisavljevic, D., Temim, T., De Looze, I., et al. 2024, arXiv:2401.02477. doi:10.48550/arXiv.2401.02477
- Millard, M. J., Ravi, A. P., Rho, J., et al. 2021, *ApJS*, 257, 36. doi:10.3847/1538-4365/ac1d4a
- Min, M. 2015, *European Physical Journal Web of Conferences*, 102, 00005. doi:10.1051/epjconf/201510200005
- Molster, F. & Kemper, C. 2005, *SSRv*, 119, 3. doi:10.1007/s11214-005-8066-x
- Molster, F. J., Waters, L. B. F. M., Trams, N. R., et al. 1999, *A&A*, 350, 163. doi:10.48550/arXiv.astro-ph/9908065
- Molster, F. J., Yamamura, I., Waters, L. B. F. M., et al. 1999, *Nature*, 401, 563. doi:10.1038/44085
- Nagahara, H., Ogawa, R., Ozawa, K., et al. 2009, *Cosmic Dust - Near and Far*, 414, 403
- Nozawa, T., Kozasa, T., Tominaga, N., et al. 2008, *ApJ*, 684, 1343. doi:10.1086/589961
- Oliva, E., Moorwood, A. F. M., Drapatz, S., et al. 1999, *A&A*, 343, 943. doi:10.48550/arXiv.astro-ph/9901254
- Ravi, A. P., Rho, J., Park, S., et al. 2023, *ApJ*, 950, 14. doi:10.3847/1538-4357/acddc
- Rho, J., Evans, A., Geballe, T. R., et al. 2021, *ApJ*, 908, 232. doi:10.3847/1538-4357/abd850
- Rho, J., Gomez, H. L., Boogert, A., et al. 2018, *MNRAS*, 479, 5101. doi:10.1093/mnras/sty1713
- Rho, J., Ravi, A. P., Slavin, J. D., et al. 2023, *ApJ*, 949, 74. doi:10.3847/1538-4357/acc392
- Sakon, I., Onaka, T., Wada, T., et al. 2009, *ApJ*, 692, 546. doi:10.1088/0004-637X/692/1/546
- Sarangi, A. & Cherchneff, I. 2013, *ApJ*, 776, 107. doi:10.1088/0004-637X/776/2/107
- Sarangi, A. & Cherchneff, I. 2015, *A&A*, 575, A95. doi:10.1051/0004-6361/201424969
- Sarangi, A., Matsuura, M., & Micelotta, E. R. 2018, *SSRv*, 214, 63. doi:10.1007/s11214-018-0492-7
- Schwarz, G. J., Shore, S. N., Starrfield, S., et al. 2007, *ApJ*, 657, 453. doi:10.1086/510661
- Schwarz, G. J., Woodward, C. E., Bode, M. F., et al. 2007, *AJ*, 134, 516. doi:10.1086/519240
- Seward, F. D., Harnden, F. R., Murdin, P., et al. 1983, *ApJ*, 267, 698. doi:10.1086/160907
- Shahbandeh, M., Sarangi, A., Temim, T., et al. 2023, *MNRAS*, 523, 6048. doi:10.1093/mnras/stad1681
- Sibthorpe, B., Ade, P. A. R., Bock, J. J., et al. 2010, *ApJ*, 719, 1553. doi:10.1088/0004-637X/719/2/1553
- Smith, J. D. T., Rudnick, L., Delaney, T., et al. 2009, *ApJ*, 693, 713. doi:10.1088/0004-637X/693/1/713
- Smith, N., Foley, R. J., & Filippenko, A. V. 2008, *ApJ*, 680, 568. doi:10.1086/587860
- Spoon, H. W. W., Tielens, A. G. G. M., Armus, L., et al. 2006, *ApJ*, 638, 759. doi:10.1086/498566
- Sturm, B., Bouwman, J., Henning, T., et al. 2013, *A&A*, 553, A5. doi:10.1051/0004-6361/201220243
- Sugerman, B. E. K., Ercolano, B., Barlow, M. J., et al. 2006, *Science*, 313, 196. doi:10.1126/science.1128131
- Szalai, T., Vinkó, J., Balog, Z., et al. 2011, *A&A*, 527, A61. doi:10.1051/0004-6361/201015624
- Tappe, A., Rho, J., & Reach, W. T. 2006, *ApJ*, 653, 267. doi:10.1086/508741
- Telesco, C. M., Pina, R. K., Hanna, K. T., et al. 1998, *Proc. SPIE*, 3354, 534. doi:10.1117/12.317279
- Temim, T., Dwek, E., Arendt, R. G., et al. 2017, *ApJ*, 836, 129. doi:10.3847/1538-4357/836/1/129